ARTICLE TYPE

Finite Element Modelling of Atomic Force Microscopy Imaging[†]

Joshua Giblin-Burnham,[a,b], Yousef Javanmardi[c], Emad Moeendarbary[c], and Bart W. Hoogenboom[a,b,‡]

Atomic Force Microscopy (AFM) is a versatile three-dimensional topographic technique implementing a mechanical probe to raster-scan and image sample surfaces. The technique provides reliable nanometer measurements of materials and has become a valuable tool with a diverse range of applications. However, there are limited computational recreations of AFM imaging, and the area could benefit from greater tools to aid in interpreting surface characteristics. Consequently, this research presents novel computational modelling of AFM imaging using Finite Element Modelling (FEM). Validation of the modelling focused on the indentation of elastic spheres. The results indicate that simple Hertzian models underestimate the elastic modulus of spherical samples and require Double Contact models. FEM was applied to analyse the perceived compression of simple hemispheres and periodic surfaces during AFM imaging. These simulations highlighted the dependency of the elastic behaviour on the contact radius and tip convolution. Our results indicated that larger indenters require larger forces to compress the sample to the same extent. In addition, Fourier analysis of the simulated AFM contours elucidated a possible novel trend, that larger indentation forces recover more of a surface's periodicity. These simulations show the viability of the FEM approach in reproducing the AFM dynamics and provide a wealth of extensions to be explored.

1 Introduction

Atomic Force Microscopy (AFM) is a versatile three-dimensional topographic technique implementing a mechanical probe to raster-scan and image sample surfaces. The technique provides reliable nanometer measurements of materials [1–4] and has become a valuable tool with a diverse range of applications in areas such as materials physics, nanotechnology, electronics, and biology [3,5,6]. In addition, AFM can image under natural conditions, such as in aqueous solutions and in real-time, allowing imaging of cell dynamics and biological processes. This includes imaging protein unfolding [7] and conformational changes [8], alongside, characterising microbial surfaces [9,10]. The ability to image and measure the physical properties of microbial surfaces can give important insight into microbiology, such as improving inhibition and cellular damage produced by antimicrobial compounds [9,11].

However, there are limited computational recreations of AFM imaging, and the area could benefit from greater tools to aid in interpreting surface characteristics. As with any experimental technique, AFM has limitations. Various effects can lead to ambiguity in images and image artefacts. A key source of error is a consequence of the resolution being directly dependent on imaging force and the probe geometry [12]. Imaging with large forces can dramatically reduce image resolution and damage the surface. Furthermore, probe geometry and its interaction with the sample is important to image contrast [12]. An AFM image is a convolution of the probe geometry and the sample's topology. Therefore, the tip-sample convolution produces a trace of the tip geometry over the surface, broadening protrusions and narrowing holes in the surface. Furthermore, other errors may arise due to environmental surroundings. For example, environmental vibrations can cause the probe to vibrate and produce artefacts and blur. Similarly, thermal drift is produced from prolonged usage, which causes the probe to expand/ contract thermally and produce deviations in the system.

Currently, simulations of AFM imaging use a hard-sphere model and neglect tip indentation. Recent work by Amyot R, Flechsig H et al.. [13] produced the BiomolecularAFMviewer which, similar to this project, uses protein structural data to simulate AFM images. This has proven the utility in interpreting experimental observa-

[a] London Centre for Nanotechnology, University College London, 17-19 Gordon Street, London WC1H 0AH.

[b] Department of Physics and Astronomy, University College London, Gower Street, London WC1E 6BT.

[c] Department of Mechanical Engineering, University College London, Gower Street, London WC1E 6BT.

[†] Electronic Supplementary Information (ESI) available: []. See DOI: 10.1039/cXsm00000x/

[‡] b.hoogenboom@ucl.ac.uk

tions and reconstruct resolution-limited experimental images[14]. However, the simulations do not account for indentation into the surface, surface deflection, off-axial forces that produce sliding and friction, or elastic properties of the surface. This approach could be improved by accounting for force curves and the indentation of the tip with elastic properties of the material.

Other computational simulations of AFM have been used to produce such force curves that reflect these properties. However, these applications study quantitative AFM results as opposed to imaging[15–19]. Previous work has shown the viability of the commercial software ABAQUS and Finite Element Modelling (FEM) in the study of indention in AFM; Liu *et al.*[15] validated a FEM model with less than 10% error when comparing the simulated force-indentation curves with the experimental data. The work by Rajabifar *et al.*.[20] simulated the viscoelasticity contact between an AFM tip and a surface showing a fast and accurate use of FEM to simulate AFM indentation and the associated force curves.

Our research presents novel FEM and computational methods to model and explore AFM images, specifically in biomolecular samples. The primary work of this research focuses on improving the modelling of previous AFM simulations from a hard sphere model to a model with tip surface interactions. FEM simulations enable us to simulate tip indentation and generate force curves that incorporate more intricate forces and dynamics. We employ several FEM simulations to investigate contact models of indentation and sample compression in AFM imaging. The overall goal was to produce more accurate images and artefacts. Our implementation of FEM utilises the commercial engineering software ABAQUS.

2 Methodology

2.1 Simulation of AFM Imaging

Simulating AFM images requires the calculation of contours of constant indentation force across a sample. Using Finite Element Modelling (FEM), the sample surface and probe tip geometry are recreated, and AFM raster scan dynamics are replicated by performing independent indentations across the surface. Biological structures are produced using Protein Data Bank (PDB) files with geometric dimensions in Å. For simplicity, the biomolecule is modelled as an elastic material produced from the assembly of the individual atoms (with van der Waals radius). The molecule is partially embedded in a rigid base/ substrate and fixed at its base to simulate a soft molecule absorbed onto a solid support.

Scan positions are determined by subdividing the XY domain and calculating corresponding initial indenter heights. Initial heights are computed from hard-sphere/ tangential contact points, ensuring consistent indentation depths across the surface. The tangent points between the surfaces are calculated by setting the tip above the sample and determining the minimum vertical distance between the tip and the molecule's surface. Figure 1D illustrates the calculations. By computing the vertical distances between the indenter's surface and atoms within the indenter's boundary ($R_{Boundary}$), an array of height differences (ΔZ) is obtained. Figure 1C illustrates that the minimum ΔZ value corresponds to the tangential contact position.

Extracting simulated vertical forces and displacements produces a four-dimensional array of indenter positions and forces. Subsequently, contours are computed using a reference force, generating the final AFM images. Contours are calculated from force-indentation data via list comprehension, extracting the depth at which the indentation force exceeds a given reference force. Linear or power normalisation is applied depending on detail contrast, and images are interpolated using bi-cubic interpolation to increase pixel density.

2.2 Model Formulations and Validation

Simulations implemented ABAQUS (2017) software for quasi-static, implicit computations using user subroutines UMAT. Samples are modelled as continuous, homogeneous and isotropic elastic materials with Young's modulus and Poisson ratio comparable to biomolecules . To eliminate the hourglass effect, R3D10 tetrahedral elements are employed . Simulations impliment "surface to surface contact" interaction with "hard", nonadhesive normal contact and "rough" (Coulomb friction), non-slip tangential contact.

The shape of a blunt AFM tip, presented in Figure 1A, is a simplified construct similar to the SEM image of actual AFM tips shown by Chen *et al.*[21]. The tip is modelled as a rigid (incompressible) cone with opening angle $\theta = 20^o$ ending in a spherical termination of radius R[22]. The spherical portion smoothly transitions to the conical segment at the tangential contact point described by,

$$X_{tangent} = R\cos\theta$$
$$Y_{tangent} = R(1 - \sin\theta) \tag{1}$$

Therefore, the tip can be considered spherical for indentations $\delta/R < 1 - \sin(\theta) \approx 0.65$, which allows for a direct comparison with analytical indentation models. These theoretical indentation models characterise the behaviour of the simulated indentation. The Hertz model describes contact between a sphere and an elastic half-space, defining the indentation force, F[23–25],

$$F_{Hertz}(\delta_{12}) = \frac{4}{3}\frac{E}{(1-\nu^2)}\sqrt{R^*}\delta_{12}^{3/2} \tag{2}$$

for indentation depth δ_{12}, Young's modulus E, Poisson's ratio ν, and tip-surface contact radius R^*. Where $\frac{1}{R^*} = \frac{1}{R} + \frac{1}{r}$, with indenter radius R and surface radius r. Applying the Hertzian analysis to conical indenters, we recover the Sneddon model. For spherical samples, a modified Sneddon model developed by Han *et al.*[16] is given as,

$$F_{Sneddon}(\delta_{12}) = \frac{2}{\pi}\frac{E}{(1-\nu^2)}\cdot tan(\theta)\delta^2 \cdot f\left(\frac{\delta}{2r}\right) \tag{3}$$

$$f\left(\frac{\delta}{2r}\right) = 1 + \gamma\left(\frac{\delta}{2r}\right) \tag{4}$$

$$\gamma = -5.103\nu^2 - 13.99\nu + 13.53 \tag{5}$$

where θ is the indenters principle angle. However, as shown

by Glaubitz *et al.* [26], compression of soft spherical samples during indentation leads to significant underestimations of Young's modulus when analysing the AFM force curves with the simple Hertz model. "Double Contact" models [26,27] account for compression produced by spherical indenters as such,

$$F_{Double}(\delta_{12}) = \frac{4}{3}\frac{E}{(1-\nu^2)}\left[\frac{(R^*r)^{1/3}}{R^{*1/3}+r^{1/3}}\right]^{3/2}\delta_{12}^{3/2} \quad (6)$$

Applying ABAQUS to AFM indentation into elastic spheres of varying radii provides a robust validation of simulation accuracy through comparison with the theoretical contact models. Following the common experimental determination of Young modulus *et al.* [18,28–31], theoretical contact models are used to fit the Young modulus for simulated indentation force curves of elastic spheres. The elastic sphere moves freely with a fixed, rigid base beneath. Restricting indentation to the z-axis allows the modelling to be asymmetrically centred around the z-axis.
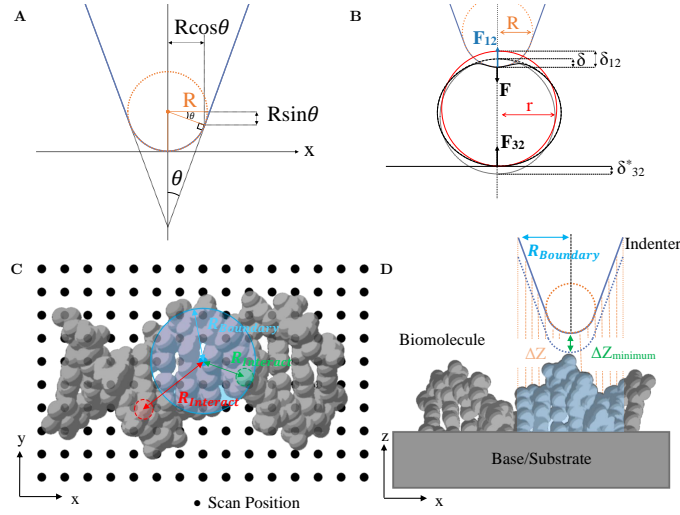

Fig. 1 (A) Illustration of AFM tip geometry as a rigid cone with opening angle θ ending in a spherical termination of radius R. (B) ABAQUS model assembly from elastic indentation tests. Modelled asymmetrically using elastic spheres modelled as semi-circles with a rigid base beneath. (C-D)Schematic diagrams illustrating the calculation of initial scan heights in AFM code. (C) Illustration of the calculation atoms on the surface within the indenters boundary. Black dots represent the XY grid of scan positions. The calculation is restricted to the XY plane in which only atoms inside the radial extent of the indenters, $R_{Boundary}$ (blue), are calculated. The red atom represents an atom outside the extent and thus is omitted, as appose to the green atom, which is included. (D) Illustration of calculation of heights for each given position. An array of all distances (ΔZ) between the indenters and molecules surfaces are calculated (red). The minima of these distances thus give the translation distance to place the indenter in tangential contact.

3 Results and Discussion

3.1 Validation of FEM Against Analytical Indentation Models

First, the indentation into an elastic sphere tests and validates our FEM approach. Indentation of the AFM tip into the soft spherical sample, with elastic modulus $E = 1000\text{kPa}$, exerts a compressive force **F** onto the sample. Illustrated in Figure 2A, the compression of the sphere enhances the perceived indentation depth, δ_{12}, and indentation force is distributed between the reaction at the base

and the indenter such that the perceived force, F_{12}, is diminished.

Figure 2B shows the extracted force-indentation data for various surface-indenter ratios $\frac{r}{R}$ scaled in dimensionless units. The simulations show the characteristic indentation force curve. Increasing the surface radius (R) decreases the bounded area, indicating heightened energy requirements for compressing smaller spheres. These more complex compression dynamics are expected to deviate from the theoretical models, which model linear elastic responses [31]. The compression necessitates the Double Contact model, which more accurately models AFM indentations.

The dimensionless force, $\frac{F}{E^*R^2}$, as it varies with relative indentation depth, $\frac{r}{R}$, is fitted to the theoretical models as shown in Figure 2C. The Double Contact and Hertz model produced qualitatively tight fits. In contrast, the Sneddon model displays more pronounced curvature, overestimating the deformation from the spherical AFM tip compared to a sharper conical tip. Moreover, model accuracy across various surface radii (r) can be assessed by comparing the measured Young's modulus (E_{AFM}), extracted as a fitting parameter [28,29,31], with the true Young's modulus of the sample.

The Hertzian model underestimates Young's modulus, shown in Figure 2D, underfitting by approximately half across surface range. This reduction is consistent with the decrease in indenter reaction force experienced when compressing the sample. The Sneddon model shows a poor fit, converges to zero, indicating the spherical indentation is dominant which is consistent with the relative size of the spherical termination.
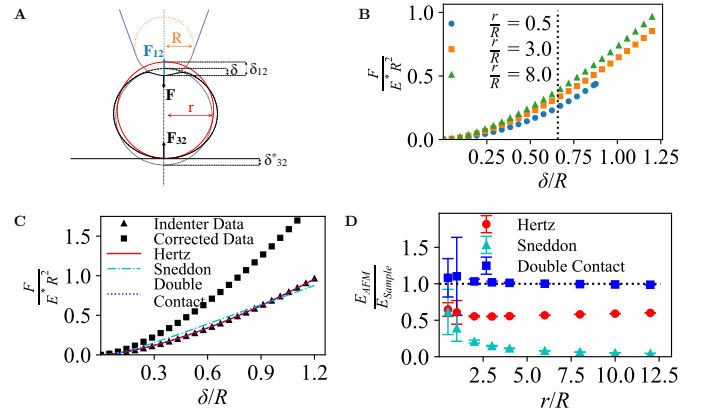

Fig. 2 (A) Illustration of double contact experienced by spherical sample. For indentation δ, indenter displacement δ_{12}, surface compression δ_{32}^*, indentation force F, indenter reaction force F_{12}, and base reaction force F_{32}. Corrected values for the indentation depth, δ, are calculated by subtracting the surface compression at its base, δ_{32}^*, from the indenter's displacement δ_{12}. (B) Force curve for indentation δ/R into the elastic sphere of varying radius, r/R. (C) Plot of fitted contact models over dimensionless force, $\frac{F}{E^*R^2}$, against relative indentation, $\frac{\delta}{r}$ range. For surface-indenter ratios, $r/R = 3.0$. (D) Variation of relative Young's Modulus, $\frac{E_{AFM}}{E_{Sample}}$ for varying surface-indenter ratios, r/R.

In comparison, the Double Contact models converge to the expected Young's modulus within the confidence interval. At small surface radii, the AFM tip is comparable size to the surface. Force are distributed over substantial portion of the surface producing excessive compression and shear forces. Consequently, this causes significant errors and deviation from the theoretical models along

with the contradiction of the assumption of infinite surface extent. The error decreases as surface radius increases and compressive effects lessen although a minor offset is expected due to the indenters conical portion. Overall, these results further validated our ABAQUS modelling.

3.2 FEM Simulation of Compression Along Single AFM Scanline

3.2.1 Analysis of Hemisphere Structure

Next, to establish how AFM measures the topography and nanomechanics of simple geometries, we probed imaging of elastic hemispheres. Simulations focused on the perceived compression of the structure's central scanline. The spherical/cylindrical structures model the two-dimensional compression of DNA imaging along the transverse axis [32,33]. The hemisphere is modelled as a three-dimensional elastic part in ABAQUS with a fixed, rigid base beneath. Unlike the indentation of a full sphere with a single contact point at the base, the fixed base of a hemisphere alleviates the compression of the surface. This produces less ambiguity as the elastic response follows the Hertzian model and negates the consideration of typical double contact required for a full sphere.

As illustrated in Figure3A, except when indenting the very centre of the hemisphere, the AFM tip will first contact the hemisphere laterally such that the experienced force and tip coordinates are offset. Consequently, this effect broadens the apparent surface depending on the hard-sphere/ tangential contact. Shown in Figure 3B, C are results for a sharp and blunt tip, respectively. The figures show heat maps of the indentation force across the cross-section of the scan line. Subsequently, the AFM appearance for a given reference force is produced from the corresponding contour of equal force, fitted using a smooth 2D cubic spline.

As is common in nanomechanical analysis by AFM [28,29,31], we quantify the surface stiffness by fitting the force-indentation curves, clipped to equal depths, by Hertz model (Equation 2). This yields an effective Youngs modulus, $\frac{E_{AFM}}{E_{Sample}}$, as a function of relative lateral position, x/R, shown in Figure 3D. Due to the geometry, the indentation of the centre has the greatest contact radius and surface extent below; consequently, the elastic response is more significant. Conversely, indentations along the sides of the hemisphere are softer due to a smaller contact radius and uneven tangential force. Moreover, as the indentation force varies as a function of the contact radius, the variation in Young's modulus over the scan position emulates the same broadening as in the apparent topography. Larger indenters produce a flatter fitted Young's modulus highlighting that a greater effective stiffness is experienced at larger indenter-surface ratios.

However, as shown in Figure 3E, these effects depend on the depth of surface indentation. Fitting indentation data clipped to given depths produces the effective Young's modulus for the corresponding indentation force. As force/ depth increases, the measured Young's modulus approximates the sample's value more closely. At the centre, all indenters converge on an overfit value; conversely, the softened response along the edge is further highlighted in under-fitted values.

To quantify the lateral resolution/ apparent width of the hemi-

sphere for varying imaging force, we analyse the Full Width Half Maxima(FWHM) [32]. FWHM is calculated from the roots of the contour splines at half the maximum value. Figure 3F shows FWHM decreases asymptotically as the indentation force decreases. As the force increases, the sample is indented to greater depth producing tighter, compressed force contours and narrowing the surface's appearance. As noted in similar experimental work on spherical nanoparticles by Junno *et al.* [34], as AFM images are convolutions of the samples and tip geometries, FWHM is not directly indicative of image accuracy, and an overestimated is expected.
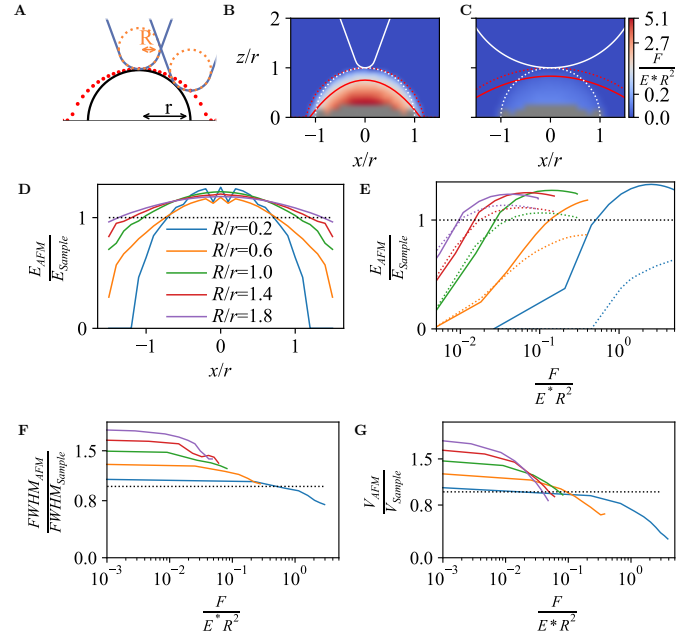

Fig. 3 (A) Geometry of scan along the central axis of a hemisphere. Three-dimensional geometry is produced by rotating the indenter and semi-circle around the central z-axis. The hemisphere is shown in black with a radius r. Indenter geometry is shown in blue, with the circular tip of radius R in orange. Red points indicate initial scan positions (Hard sphere contact points). (B) Interpolated two-dimensional heat map of indentation force over the scanning axis for hemisphere structure with indenter $R/r = 0.2$. Including overlayed contour of constant force, $\frac{F}{E^*R^2} = 0.227$, shown in solid red. The indenter is solid white, and the surface is dotted white. Points of zero force/ hard sphere contact are shown in dotted red. A mask excludes positions with no indentation data shown in grey. (C) Interpolated two-dimensional heat map of indentation force over the scanning axis for hemisphere structure with indenter $R/r = 1.4$. Including overlayed contour of constant force, $\frac{F}{E^*R^2} = 0.227$, shown in solid red. The indenter is solid white, and the surface is dotted white. Points of zero force/ hard sphere contact are shown in dotted red. A mask excludes positions with no indentation data shown in grey. (D) Apparent Young's modulus measured across scan positions for each indenter radius (R/r). (E) Apparent Young's modulus variation over contour force for each indenter radius(R/r). Measured at the centre (solid line) and at the surface edge (dashed). (F) Relative FWHM of the contour divided by FWHM of true geometry ($FWHM^* = \frac{FWHM_{AFM}}{FWHM_{Sample}}$) variation over contour force for each indenter radius(R/r). (G) Volume variation over contour force in spherical structures for each indenter radius(R/r).

A similar analysis of the measured volume shows that the tip convolution overestimated the hemisphere volume. Volume is calculated using discrete, numerical integrals of contour splines. As the indentation force increases, more significant compression re-

duces the apparent appearance. As indenter size decreases, larger forces are required to achieve the same relative decrease in volume. This is expected as smaller indenters have smaller contact areas and complement experimental volumetric measurements of protein complexes with AFM[35,36].

Overall, the data illustrate how strongly the measured topography and nanomechanics may depend on tip and sample geometry and the applied forces in an AFM experiment. Analysis of the compression displayed that increasing the indenter-to-surface ratio results in lower indentation forces. As the surface-indenter ratio/contact radius increases, the forces are spread over a larger area, resulting in less deformation for the same force.

3.2.2 Analysis of a Simple Periodic Structure

AFM resolution is commonly indicated by reference to structures that are at least locally periodic, for example, in atomic resolution mapping at a solid-liquid interface[37], in identification of recurrent features in a two-dimensional lattice of membrane proteins[38,39], or the distinction of the two strands of the double helix along a DNA molecule[40]. Therefore, we next considered AFM measurements on a periodic soft material. As shown in Figure 4, the structure has a wavelength $\lambda = 10nm$ and amplitude, $A_{Sample} = 10nm$. Except when indenting the peak, the AFM tip will contact the structure laterally. This broadens the wave crest similar to the hemisphere, alongside the simultaneous reduction in trough depth, visible when comparing the sharp and blunt tip heat maps shown in Figure 4B, C, respectively.

Unlike for the hemisphere, the contact produces an inverse relationship in perceived Young's modulus across the scan positions, shown in Figure 4D. At the surface trough, $x/\lambda = 0.5$, the indenter experiences lateral contact from the surface on both sides producing maximum surface interaction and a larger effective stiffness/ Young's modulus. However, the contact radius decreases for scans away from wave trough and forces are distributed laterally. Therefore, Young's modulus decreases proportionally up to the crest at $x/\lambda \approx 0$. As shown in Figure 3E, Young's moduli generally converge true surface at the wave crest. Conversely, at the trough across most of the range, increasing force produces a more significant deviation in perceived Young's modulus.

As shown in Figure4F, as before, the tip convolution leads to overestimating the FWHM. At sufficiently high forces, the measured FWHM approaches the sample FWHM. However, the much softer gradient compared to the hemisphere indicate lower compression around the wave's midpoint and large force required to indent the slope region. Moreover, Figure 4G shows much less prominent volume variation than the hemisphere. For each indenter, there is only a slight reduction in volume as the indentation force increases, and, unlike the hemisphere, apparent volume is not directly proportional to indenter radius. As volume is measured from the peak to the trough, the composite reduction in trough depth results in a smaller volume as the indenter radius increases from $R/\lambda = 0.15$.

These results, especially FWHM and volume, indicate that the apparent sharpness of features may increase at higher forces. However, an increase in resolution could be artifactual[41]. Spatial resolution in wave-based microscopy is often quantified by

considering the spatial frequencies[41–44], wave numbers k, here expressed in units of $2\pi/\lambda$. We fit data to a Fourier series to quantify the spatial resolution of the contours and show that the same phenomenon occurs for the indented surface. As the surface and contours are symmetric functions, Fourier analysis only requires the cosine terms, modulated by individual amplitude, A_k, and frequency, $2\pi k$, given by,

$$g(x) \approx \sum_{k=0}^{\infty} A_k \cos\left(\frac{2\pi k x}{\lambda}\right) \qquad (7)$$
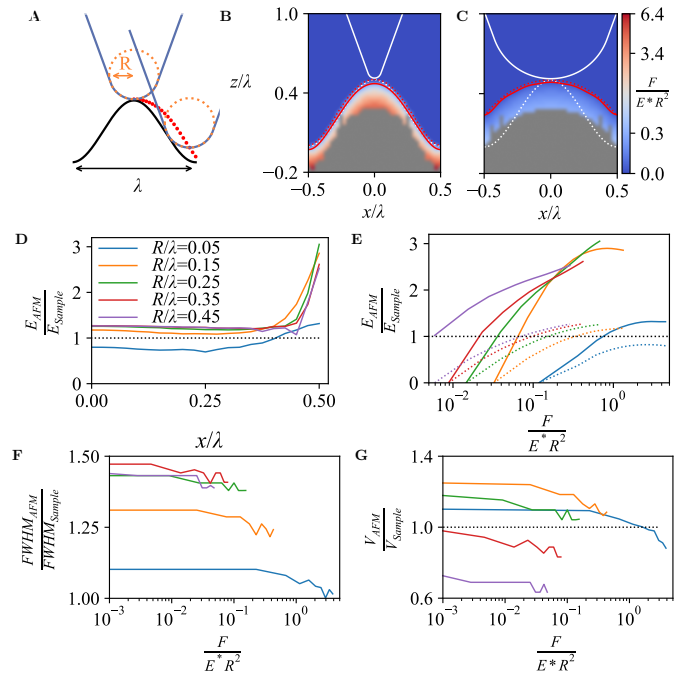

Fig. 4 (A) Geometry of scan along the central axis of a hemisphere. Three-dimensional geometry is produced by rotating the indenter and extruding the wave. Wave is shown in black with wavelength λ. Indenter geometry is shown in blue with a circular tip of radius R in orange. Red points indicate initial scan positions (Hard sphere contact points). (B) Interpolated two-dimensional heat map of indentation force over the scanning axis for periodic structure with indenter $R/\lambda = 0.05$. Including overlayed contour of constant force, $\frac{F}{E^*R^2} = 0.227$, shown in solid red. The indenter is solid white, and the surface is dotted white. Points of zero force/ hard sphere contact are shown in dotted red. (C) Interpolated two-dimensional heat map of indentation force over the scanning axis for periodic structure with indenter $R/\lambda = 0.45$. Including overlayed contour of constant force, $\frac{F}{E^*R^2} = 0.227$, shown in solid red. The indenter is solid white, and the surface is dotted white. Points of zero force/ hard sphere contact are shown in dotted red. (D) Fitted Young's modulus over scan positions for each indenter radius (R/λ). (E) Apparent Young's modulus variation over contour force for each indenter radius(R/λ). Measured at trough (solid line) and at crest (dashed). (F) Relative FWHM of the contour ($FWHM^* = \frac{FWHM_{AFM}}{FWHM_{Sample}}$) variation over contour force for each indenter radius($\frac{R}{\lambda}$). (G) Volume variation over contour force in spherical structures for each indenter radius(R/λ).

The individual contribution highlights the deviation and behaviour of the surface when indented. Figure 5B shows an illustrative plot of the Fourier component's amplitudes for corresponding frequencies. The zeroth component of the Fourier series represents a linear vertical offset. The increasing trend corresponds to an increased trough height for larger indenter-surface ratios.

The first component corresponds to surface periodicity and is expected for the contours that match the surface's geometry ($A_k = 1$ for $k = 1$ and zero for $k \neq 1$), as shown by the black bar. The decreasing amplitude of this component corresponds to an increase in surface distortion, as the amplitude is shared proportionally with higher-order terms. The second component is the significant component producing the widening wave peak, and higher-order terms refine the curvature of the contour.

Therefore, the deviation from the true surface geometry and accuracy of the imaging can be quantified by analysing the variation of the first Fourier component over a range of contour forces. Analysing the absolute A1 for each contour force, shown in 5C, indicates how well we extract information from the surface topography. A lower indenter-surface ratio produces less apparent structure deviation as the scan/tip more closely follows the surface geometry. Moreover, A1 is generally constant over the range of contour forces.

In contrast, the relative variation of higher order component $\sum_{k>1}^{N} A_k$, shown in Figure 5D, indicates that although the relative value of the first component may be constant throughout the forces range, the percentage of anomalous higher order terms in the series does decrease. As these higher-order terms are linked to errors in contour shape, this suggests a greater percentage of the periodicity of the surface is recovered. This indicates that the apparent resolution extracted from the AFM image increases with indentation force. This could be due to the increased proportion of the indenter in contact with the surface and the elastic behaviour becoming more linear for deeper/high-force indentations. As a result, the indentations are subject to more influence from the surfaces and better resolved topological variation.

Overall, this illustrates how strongly the measured topography and nanomechanics may depend on tip and sample geometry and the applied forces in an AFM experiment. As before, the volume highlights that the larger indenters/contact areas require larger forces to compress the sample to the same extent as smaller indenters. However, the Fourier analysis elucidates a possible novel feature, demonstrating that larger indentation forces recover more surface periodicity.

4 Conclusion

Our FEM approach has demonstrated some novel and varied applications for the analysis of AFM imaging. Our analysis of the contact models for elastic half-spaces and spheres agreed with the theoretical models. Most prominently, the results highlight the under-fitting of the elastic modulus produced by simple Hertzian models for spherical samples. Moreover, our novel formulation of the Double Contact model for conical indenters demonstrated good predictive power over a range of surface radii.

Moreover, applying FEM to analyse the compression of hemispheres and simple periodic surfaces highlighted the quantitative power of this approach. These simulations highlighted the dependency of the elastic behaviour on the contact radius and tip convolution. Our results indicated that larger indenters require larger forces to compress the sample to the same extent. In addition, Fourier analysis of the simulated AFM contours elucidated a possible novel trend that larger indentation forces recover more
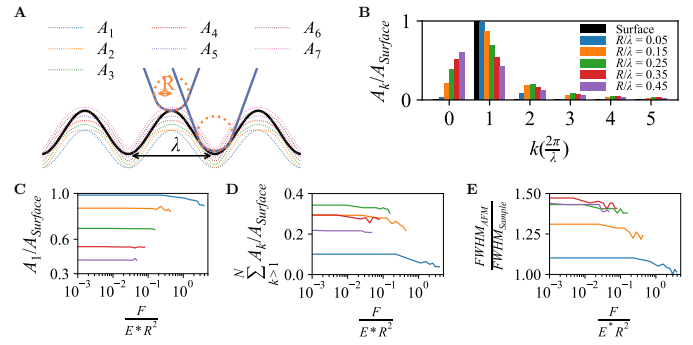

Fig. 5 Analysis of force contours for a periodic structure. (A) Geometry of scan along the central axis of a hemisphere. Three-dimensional geometry is produced by rotating the indenter and extruding the wave. Wave is shown in black with wavelength λ. Indenter geometry is shown in blue with a circular tip of radius R in orange. Illustration of Fourier decomposition for hard sphere contour show as dashed lines. (B) Fourier Series Component for force contours at $\frac{F}{E*R^2} = 0.227$. (C) Variation of relative component A_1/A_{Sample} over contour force for a range of indenters ($\frac{R}{\lambda}$). (D) Relative variation of higher order component $\sum_{k>1}^{N} A_k$ over contour force for range of indenters ($\frac{R}{\lambda}$). (E) Variation of relative FWHM over contour force for each indenter radius ($\frac{R}{\lambda}$).

of a surface's periodicity.

Conflicts of interest

There are no conflicts to declare.

Acknowledgements

Notes and references

1 N. Nagashima, S. Matsuoka and K. Miyahara, *JSME international journal. Ser. A, Mechanics and material engineering*, 1996, **39**, 456–462.

2 M. Kempf, M. Göken and H. Vehoff, *Applied Physics A: Materials Science & Processing*, 1998, **66**, 1043–1052.

3 M. Göken and M. Kempf, *Acta Materialia*, 1999, **47**, 1043–1052.

4 A. Yamamoto, A. Watanabe, H. Tsubakino and S. Fukumoto, *Materials science forum*, 2000, **350**, 241–246.

5 N. Jalili and K. Laxminarayana, *Mechatronics*, 2004, **14**, 907–945.

6 N. C. Santos and M. A. Castanho, *Biophysical Chemistry*, 2004, **107**, 133–149.

7 M. L. Hughes and L. Dougan, *Reports on Progress in Physics*, 2016, **79**, 076601.

8 J. Moody and S. Allen, *Chemical Biology Applications and Techniques, Larijani B., Rosser, CA, Woscholski, R., Eds. John Wiley & Sons, Ltd., Hoboken, NJ, USA*, 2006, 29–45.

9 C. J. Wright and I. Armstrong, *Surface and Interface Analysis*, 2006, **38**, 1419–1428.

10 Y. F. Dufrêne, *Nature Reviews Microbiology*, 2004, **2**, 451–460.

11 A. K. Tyagi and A. Malik, *Micron*, 2010, **41**, 797–805.

12 Y. F. Dufrêne, *Journal of bacteriology*, 2002, **184**, 5205–5213.

13 R. Amyot and H. Flechsig, *PLoS computational biology*, 2020, **16**, e1008444.

14 R. Amyot, A. Marchesi, C. M. Franz, I. Casuso and H. Flechsig, *PLoS computational biology*, 2022, **18**, e1009970.

15 Y. Liu, K. Mollaeian and J. Ren, *Micron*, 2019, **116**, 108–115.

16 R. Han and J. Chen, *Journal of Materials Research*, 2021, **36**, 1762–1771.

17 C. Roduit, S. Sekatski, G. Dietler, S. Catsicas, F. Lafont and S. Kasas, *Biophysical journal*, 2009, **97**, 674–677.

18 S. Kontomaris and A. Malamou, *Materials Research Express*, 2020, **7**, 033001.

19 Y. Senda, J. Blomqvist and R. M. Nieminen, *Journal of Physics: Condensed Matter*, 2016, **28**, 375001.

20 B. Rajabifar, R. Wagner and A. Raman, *Materials Research Express*, 2021, **8**, 095304.

21 Z. Chen, J. Luo, I. Doudevski, S. Erten and S. H. Kim, *Microscopy and Microanalysis*, 2019, **25**, 1106–1111.

22 J. Canet-Ferrer, E. Coronado, A. Forment-Aliaga and E. Pinilla-Cienfuegos, *Nanotechnology*, 2014, **25**, 395703.

23 H. Hertz, *J Reine Angew, Math*, 1881, **92**, 156–171.

24 H. Hertz, *Miscellaneous papers*, 1882, 146–183.

25 H. Hertz, *Miscellaneous papers*, 1896, 146–183.

26 M. Glaubitz, N. Medvedev, D. Pussak, L. Hartmann, S. Schmidt, C. A. Helm and M. Delcea, *Soft Matter*, 2014, **10**, 6732–6741.

27 M. E. Dokukin, N. V. Guz and I. Sokolov, *Biophysical journal*, 2013, **104**, 2123–2131.

28 W. Sun, P. Yin, C. Wang, Y. Ren, X. Han, C. Wu and W. Zhang, *Journal of Materials Science*, 2021, **56**, 18210–18218.

29 E. K. Dimitriadis, F. Horkay, J. Maresca, B. Kachar and R. S. Chadwick, *Biophysical journal*, 2002, **82**, 2798–2810.

30 A. Vinckier and G. Semenza, *FEBS letters*, 1998, **430**, 12–16.

31 S. Kontomaris, A. Stylianou, K. Nikita and A. Malamou, *Materials Research Express*, 2019, **6**, 115410.

32 J. Sotres and A. Baró, *Biophysical journal*, 2010, **98**, 1995–2004.

33 K. Li, S. Du, S. Van Ginkel and Y. Chen, *Nanomaterial: Impacts on Cell Biology and Medicine*, 2014, 93–109.

34 T. Junno, K. Deppert, L. Montelius and L. Samuelson, *Applied Physics Letters*, 1995, **66**, 3627–3629.

35 Y. Wu, Y. Hu, J. Cai, S. Ma, X. Wang and Y. Chen, *Scanning*, 2008, **30**, 426–432.

36 M. E. Fuentes-Perez, M. S. Dillingham and F. Moreno-Herrero, *Methods*, 2013, **60**, 113–121.

37 T. Fukuma and R. Garcia, *ACS nano*, 2018, **12**, 11785–11797.

38 C. A. Bippes and D. J. Muller, *Reports on Progress in Physics*, 2011, **74**, 086601.

39 G. Li, N. Xi and D. H. Wang, *Journal of cellular biochemistry*, 2006, **97**, 1191–1197.

40 A. Pyne, R. Thompson, C. Leung, D. Roy and B. W. Hoogenboom, *Small*, 2014, **10**, 3257–3261.

41 K.-i. Morigaki and A. Ohta, *Journal of power sources*, 1998, **76**, 159–166.

42 L. Novotny, B. Hecht and D. W. Pohl, *Ultramicroscopy*, 1998, **71**, 341–344.

43 M. Tolan, O. Seeck, J.-P. Schlomka, W. Press, J. Wang, S. Sinha, Z. Li, M. Rafailovich and J. Sokolov, *Physical review letters*, 1998, **81**, 2731.

44 C. Slough, W. McNairy, R. Coleman, J. Garnaes, C. Prater and P. Hansma, *Physical Review B*, 1990, **42**, 9255.

Appendix

A   Notation

- δ - Indentation depth of the indenter into surface

- F - Total force of indentation

- R - Indenter radius

- r - Surface radius

- $R^* := \frac{1}{R^*} = \frac{1}{R} + \frac{1}{r}$ - Tip-surface contact radius

- α - Indenter open-angle

- $E; E_{AFM}; E_{Sample}$ - Young's modulus

- ν_2 - Poisson's ratio of the sample

- $f(\frac{\delta}{2r})$ -

- γ -

- $V_{AFM}; V_{Sample}$ -

- $FWHM^* = \frac{FWHM_{AFM}}{FWHM_{Sample}}$ -

- λ -

- A_{Sample} -

- k -

- A_k -

- $g(x)$ -